Tumor Targeting, Trifunctional Dendritic Wedge

Ramin Dubey,[†] Swati Kushal,[†] Alexis Mollard,[‡] Lesya Vojtovich,[†] Philip Oh,[§] Michael D. Levin,[§] Jan E. Schnitzer,[§] Ilya Zharov,*[‡] and Bogdan Z. Olenyuk*[†]

[†]Department of Pharmacology and Pharmaceutical Sciences, University of Southern California, 1985 Zonal Avenue, PSC B15C, HSC 9121, Los Angeles, California 90089, United States

[‡]Department of Chemistry, University of Utah, 315 S 1400 E, Salt Lake City, Utah 84112, United States

[§]Proteogenomics Research Institute for Systems Medicine, 11107 Roselle Street, San Diego, California 92121, United States

Ⓢ Supporting Information

ABSTRACT: We report in vitro and in vivo evaluation of a newly designed trifunctional theranostic agent for targeting solid tumors. This agent combines a dendritic wedge with high boron content for boron neutron capture therapy or boron MRI, a monomethine cyanine dye for visible-light fluorescent imaging, and an integrin ligand for efficient tumor targeting. We report photophysical properties of the new agent, its cellular uptake and in vitro targeting properties. Using live animal imaging and intravital microscopy (IVM) techniques, we observed a rapid accumulation of the agent and its retention for a prolonged period of time (up to 7 days) in fully established animal models of human melanoma and murine mammary adenocarcinoma. This macromolecular theranostic agent can be used for targeted delivery of high boron load into solid tumors for future applications in boron neutron capture therapy.
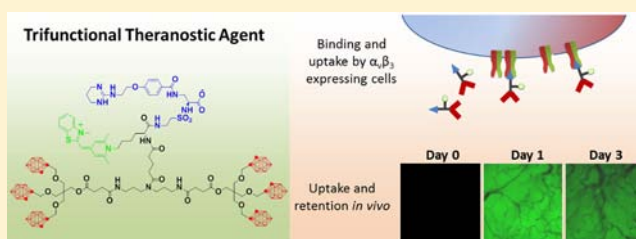
INTRODUCTION

Molecular theranostics is a novel and promising approach to tumor targeting, where a single chemical entity combines diagnostic and therapeutic modalities.[1] Such an entity could be assembled from individual therapeutic and diagnostic components, such as cytotoxic, anti-growth, or pro-apoptotic agents and contrast agents for MRI, visible-light, near-infrared, or other types of imaging. Many biocompatible materials have been proposed to serve as a platform for theranostics, including liposomes,[2−6] dendrimers,[7,8] polymers,[9−13] and nanoparticles.[10,14−23] To date, however, many such agents are nontargeted and rely on a passive transvascular delivery into the solid tumors, resulting in difficulties translating the efficacies found in vitro and in animal models into the clinic. Therefore, development of targeted theranostics capable of overcoming in vivo barriers for improved delivery and retention within tumors is needed. Herein we report a trifunctional theranostic agent designed such that its therapeutic and diagnostic modalities are combined with tumor targeting via a high-affinity integrin ligand.

Our trifunctional theranostic agent **DC-1** features a nonpeptidic integrin ligand, a monomethine cyanine dye, and a carborane dendritic wedge for BNCT (Figure 1). To combine all three modalities in one construct, we utilized scaffold based on L-lysine because it provides the necessary chemical functionalities and biocompatibility. In parallel, the dendritic wedge **DC-2**, lacking the integrin binding functionality, was designed as a nontargeted control (Figure 1).

RESULTS AND DISCUSSION

Design and Synthesis of the Conjugates. After the assessment of many available targeting strategies for tumor cells and vasculature, we narrowed our choice to high-affinity, nonpeptidic ligand for $\alpha_v\beta_3$ integrins.[24] Integrins are transmembrane receptors that mediate interactions between cells and the surrounding extracellular matrix.[28] This diverse family consists of at least 18 α and 8 β subunits that can dimerize in 24 different combinations.[29] At least 9 dimers are overexpressed in tumors with $\alpha_v\beta_3$ receptors being found in tumors and on vascular endothelial cells undergoing angiogenesis and are not typically found on quiescent cells.[30,31] A nonpeptidic RGD-mimetic ligand was selected due to its high affinity and selectivity toward $\alpha_v\beta_3$ receptors—its mean inhibitory concentration in cell adhesion assays (IC_{50}) is 40 nM for $\alpha_v\beta_3$, 5.5 μM for $\alpha_v\beta_5$, and 2.1 μM for $\alpha_{IIb}\beta_3$ integrins.[32]

As an antitumor therapeutic modality, we decided to incorporate a boron-rich moiety suitable for boron neutron capture therapy (BNCT).[33−35] BNCT is a binary treatment that has shown a promising efficacy in the recent treatment of inoperable neoplasms, especially in the locally recurred head-and-neck cancers.[36] It relies on the ability of ^{10}B nuclei to efficiently capture epithermal neutrons and to undergo the subsequent decay, releasing high linear energy transfer particles (most notably ^{4}He and ^{7}Li). These particles are highly cytotoxic yet confined to the cell or cell vicinity where they
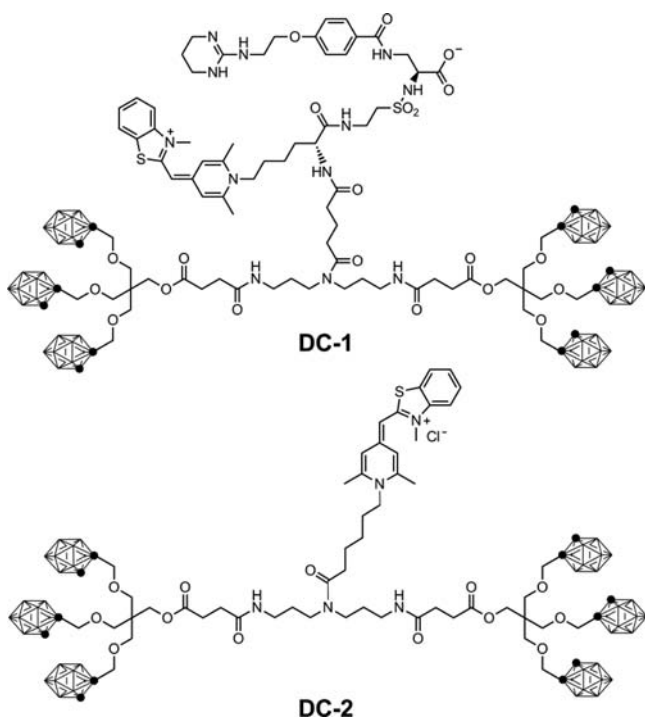
Figure 1. Structures of carboranyl dendritic wedge **DC-1** and control **DC-2**.

have been generated, as their path length is approximately equal to a cell diameter.[37] For successful BNCT, three criteria must be met: (1) low systemic toxicity and low uptake by the nontumor tissues with high tumor uptake and tumor to normal tissues and tumor to blood ratios greater than 3:1;[38] (2) [10]B must be retained in the tumor tissue but rapidly cleared from blood and normal tissues; and (3) the concentration inside or near tumorigenic cells must be $\geq 10^9$ of [10]B atoms/cell (20−35 μg [10]B/gram of tumor tissue).

In order to maximize boron content per molecule, we chose dendritic wedges built on a biocompatible scaffold that carries *o*-carboranes. Dendrimers[39] are excellent examples of the scaffolds that possess many useful properties, such as high degree of branching, multivalency, well-defined molecular weight, and biodegradability.[40−48] Dendritic wedges[49] are low molecular weight polymeric molecules that share many similarities with dendrimers, such as narrow polydispersity and reproducible pharmacokinetic behavior. The cores of dendritic wedges are less obstructed by the branches and provide a point of covalent functionalization for controlled derivatization and incorporation into modular constructs.[50] Despite the fact that dendritic wedges have smaller useful payload "capacity" compared to dendrimers of the same architecture, their structure provides for a more straightforward synthesis. Dendritic wedges also allow control over solubility, molecular weight, and, most importantly, multiplicity of therapeutic functionalities, which makes them an ideal development platform for theranostic agents.

Polyhedral boranes, such as *o*-carborane,[51,52] have high stability and high boron content, combined with the relative ease of preparation and derivatization.[53−55] To date, there have been several reports of multiple polyhedral boranes conjugated to macromolecular scaffolds such as dendrimers,[56−65] making this type of chemistry particularly attractive for our purpose. We chose tri-*o*-carboranyl pentaerythritol, whose synthesis we

previously reported,[66] as the building block of our dendritic wedge.

As a visible light imaging modality, we chose monomethine cyanine dye[67] due to its ability to emit fluorescent signal in the convenient for intravital microscopy 488−510 nm range, its photostability, and its straightforward coupling chemistry.[68] In addition, structural versatility of an environmentally sensitive monomethine cyanine group in such dyes allows for coverage of a broad range of excitation and emission wavelengths.[69,70] Such dyes typically have low fluorescence quantum yields in an aqueous solution that increase in more viscous solution or when the dye conjugate is bound to its target, primarily due to the restriction of the twisting motions around the single bond of the methine group.[69,70] This property allowed us to use cyan 40 as a local environment probe.

Syntheses of the targeted agent **DC-1** and the nontargeted conjugate **DC-2** are shown in Scheme 1 and Scheme S1 (see Supporting Information). A modular approach was chosen, where the core of the conjugate (integrin ligand connected to a linker) was synthesized first, followed by the attachment of other modules to the branched linker, as it allows additional flexibility in the type of the module. The carboxylic acid terminus of L-lysine was coupled to precursor **3** for attachment of the linker **6** which, in turn, serves to conjugate a tricarboranyl acid and the dye. First, the Boc group of the precursor **3** was removed and the resulting amine reacted with activated protected L-lysine **4** under standard peptide coupling conditions, producing conjugate **5** in excellent yield.

Subsequent deprotection of the α-amino group of the L-lysine allowed for attachment of glutaric acid-based linker **6** to give **7** in a nearly quantitative yield. After the deprotection step, the two tricarboranyl dendrons **8** were attached, and the following hydrogenation yielded the conjugate **9**, featuring a free α-amino group. The addition of AcOH, along with the use of Pd black as a catalyst, was crucial to the success of the reduction. A cyanine dye precursor (**10**) was selected based on its exclusive reactivity with primary amines via the ANRORC mechanism,[71] which is orthogonal to other present functionalities. As expected, crude **9** reacted cleanly with **10** to provide a trifunctional conjugate **DC-1** in 25% yield and >90% purity by HPLC. The identity of the conjugate was confirmed by the analysis of its ^{1}H NMR spectra and COSY as well as ^{1}H-decoupled ^{11}B NMR spectrum that displayed the expected five signals characteristic of the intact *o*-carboranes.[72] The FT-ICR HRMS spectrum of **DC-1** shows isotopic distribution in excellent agreement with the predicted pattern (SI Figures S20 and S21).

Photophysical Properties of DC-1 and DC-2. The UV−vis absorption spectra of **DC-1** and **DC-2** in DMSO and 9:1 v/v glycerol/DMSO are shown in Figure 2A and C, respectively. Both compounds showed similar spectra and the ratio of the intensities of the absorption maxima was nearly 1:1 regardless of the buffer used. The fluorescence emission intensity of conjugate **DC-1** in DMSO is low as compared to the emission in 9:1 v/v glycerol/DMSO mixture (Figure 2B). This is consistent with the low fluorescence quantum yields previously reported for unsymmetrical monomethine cyanine dyes, likely due to their twisting motions that rapidly deactivate the excited state.[73,74] In contrast, when **DC-1** is dissolved in a glycerol/DMSO mixture, a 20-fold enhancement of the fluorescence intensity is observed, presumably due to a slower twisting motion of the dye in a more viscous solvent. A similar enhancement in the fluorescence intensity was observed for

Scheme 1. Synthesis of DC-1
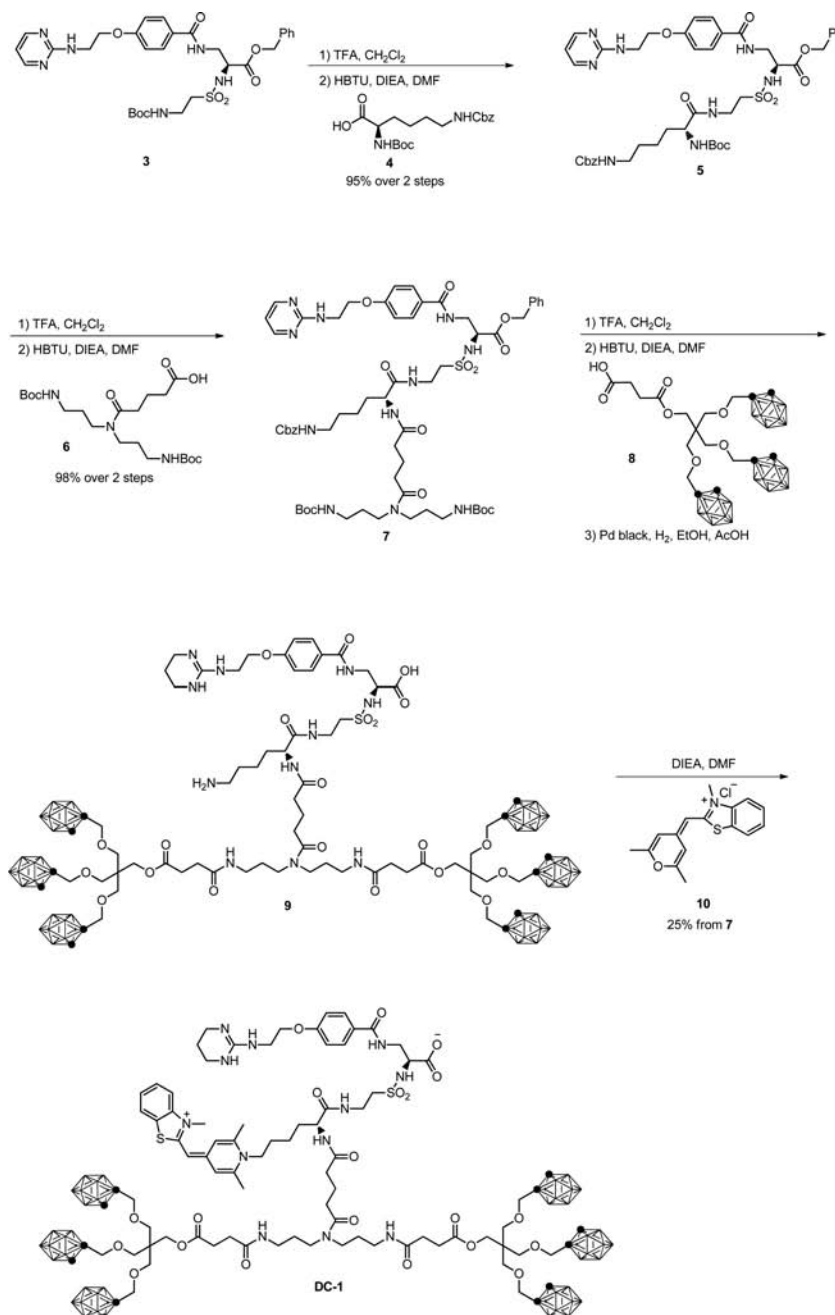
DC-2 (Figure 2D). We also measured the excitation spectra for both compound in DMSO and 9:1 v/v glycerol/DMSO with the emission wavelength being fixed at 540 nm. A similar enhancement of the fluorescence intensity was observed in the more viscous buffer (SI Figures S1 and S2).

Quantum yields of **DC-1** and **DC-2** were measured for solutions in DMSO and the 9:1 v/v glycerol/DMSO mixture using 5-carboxy fluorescein in 0.1 M aqueous NaOH as standard (quantum yield 95%).[75−77] Both **DC-1** and **DC-2** in DMSO have low quantum yields of 1.5% and 1%, respectively (SI Figure S3). However, the quantum yield of **DC-1** and **DC-2** in a viscous medium increased nearly 30-fold to 52% for DC-1 and 29% for DC-2, respectively (SI Figure S3).

In Vitro Stability Tests. A preliminary assessment of the stability was conducted in PBS (pH = 7.4) at 10 μM

concentration. The conjugate **DC-1** was incubated in PBS at 37 °C for 2 and 24 h, followed by the analysis by the LC-MS. Under these conditions we observed 98% and 85%, respectively, of the intact conjugate remaining in the solution. Our earlier X-ray crystallographic studies of the tricarboranyl pentaerythritol building block indicated that the ester groups in **DC-1** are hindered from the nucleophilic attack by the steric bulk of the tricarboranyl pentaerythritol wedge.[66] Similar results, indicating stability of **DC-1**, were obtained in DMEM and RPMI-1640 cell culture media.

Uptake of DC-1 and DC-2 by Live Cells. The uptake and intracellular localization of the targeted conjugate **DC-1** and the control compound **DC-2** in vitro was studied in WM115 and MCF7 cell lines. The cells were incubated for 14−18 h in the presence of the compounds and imaged with laser-scanning
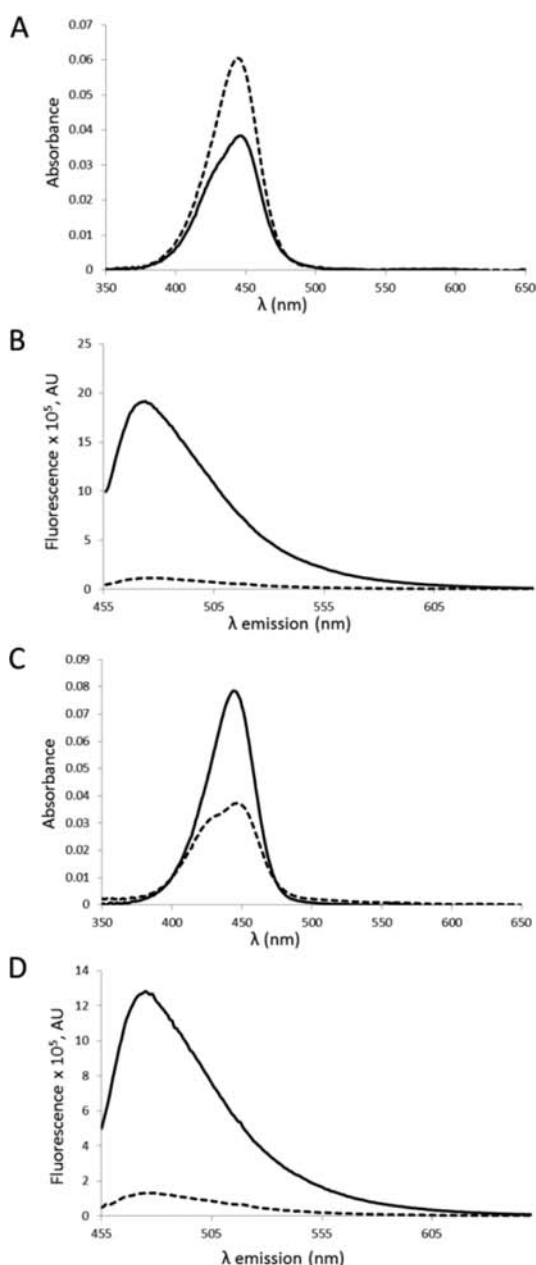
Figure 2. Absorption (A) and fluorescence emission (B) spectra of **DC-1** in solution in DMSO (dashed line) and in the more viscous medium (9:1 v/v glycerol/DMSO, solid line), and absorption (C) and fluorescence emission (D) spectra of **DC-2** in DMSO (dashed line) and in the same viscous medium. Emission spectra were recorded at $\lambda_{ex} = 450$ nm.

Figure 3. LSCM (left) and corresponding differential interference contrast (DIC, right) images of WM115 cells (A and B) and MCF7 cells (C and D) after incubation with 25 μM of **DC-1** in the cell culture medium at 37 °C (A and C) and 4 °C (B and D), respectively. WM115 cells (E) after incubation with 20 μM of **DC-2** for 14 h. Middle image: overlay of fluorescence signal with the DIC image. Images in B−D were normalized to the highest fluorescence intensity from image A. Scale bars: 20 μm.

confocal microscope (LSCM). The resulting images are presented in Figure 3. We found that at 37 °C **DC-1** localized mainly on the cell membrane and in the lysosomes of both cell lines due to the observed punctate staining, although the extent of the localization was different for each cell line.

Under the same conditions, control compound **DC-2** showed insignificant accumulation in WM115 cells (Figure 3E) and was also virtually undetectable in MCF7 cells (data not shown). Both compounds remained completely extracellular when incubated at 4 °C (Figure 3B,D). Both conjugates did not exhibit cytotoxicity as determined by staining with Sytox Orange for dead cells, observation of cell morphology, and
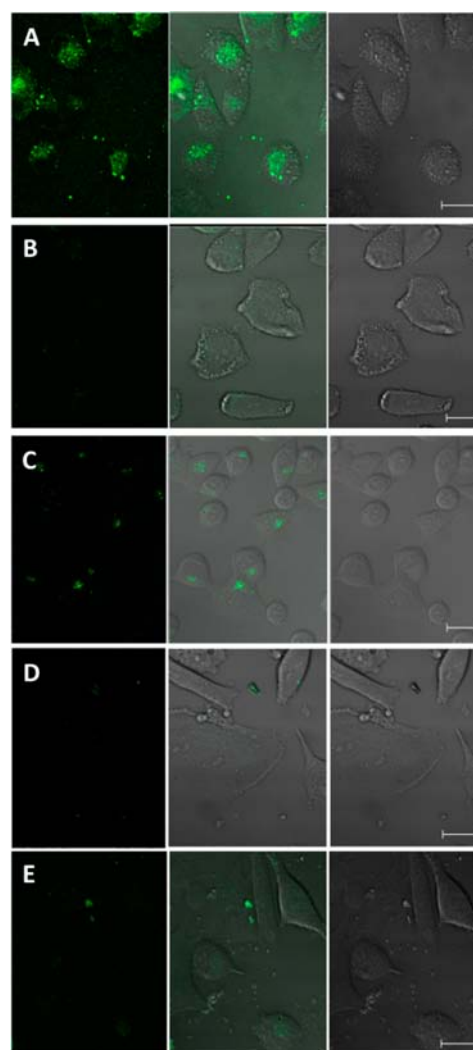
determination of the apoptosis rate by flow cytometry (vide infra).

To measure selectivity toward $\alpha_v\beta_3$ receptors in vitro, we performed blocking studies by first preincubating WM115 cells with 10 μg/mL of either anti-α_v or anti-β_3 monoclonal antibodies, followed by coincubation with **DC-1** at two different concentrations (10 μM and 25 μM). The results are summarized in Figure 4 and further detailed in SI Figure S5. The binding and internalization of **DC1** was significantly affected by the anti-α_v and completely inhibited by the anti-β_3 mAb at both concentrations (Figure 4, panels B, C, E, F and SI Figure S5, rows B, C, E, F). These results suggest that both α_v and β_3 integrin subunits play a key role in the binding of **DC-1** and its internalization. **DC-2**, as expected, did not bind or internalize regardless of the presence of the antibodies (SI Figure S6).

After observing an inhibition of uptake of **DC-1** in cells pretreated with antibodies, a competition experiment was
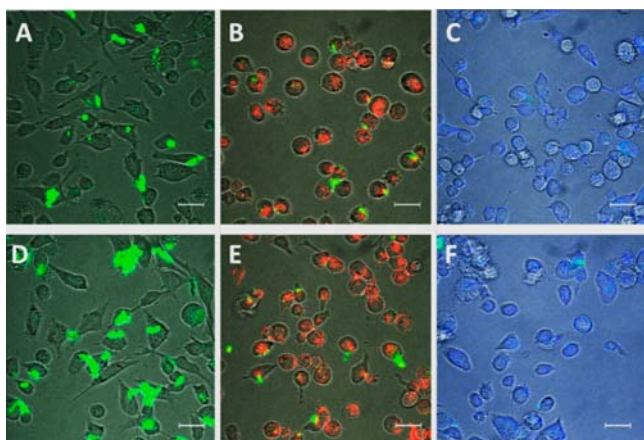
Figure 4. LSCM/DIC overlay images of anti-α_v and anti-β_3 monoclonal antibodies blocking the binding of **DC-1** in WM115 cells expressing $\alpha_v\beta_3$ integrins. (A) Cells incubated with **DC-1** (10 μM); (B) anti-α_v antibody and **DC-1** (10 μM); (C) anti-β_3 antibody and **DC-1** (10 μM); (D) **DC-1** (25 μM); (E) anti-α_v antibody and **DC-1** (25 μM); (F) anti-β_3 antibody and **DC-1** (25 μM). Antibody concentration: 10 μg/mL; scale bars: 20 μm.

performed, in which each of the antibodies and **DC-1** were added simultaneously and coincubated for 3 h (see overlays in Figure 5 and full set of images in SI Figure S7). The compound **DC-1** was added at three different concentrations (5 μM, 10 μM, and 25 μM) along with either anti-α_v or anti-β_3 antibody at
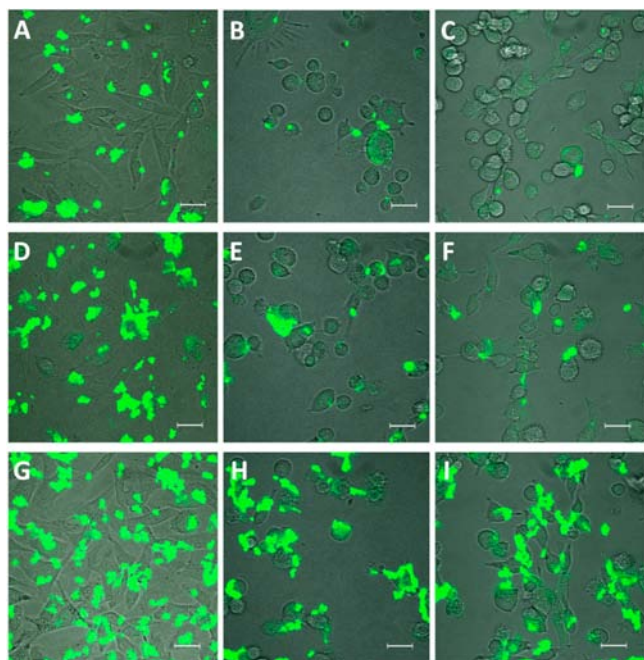
Figure 5. LSCM/DIC overlay images of the WM115 cells in a competition experiment with **DC-1** and anti-α_v or anti-β_3 antibodies. **DC-1** at three different concentrations (5 μM, 10 μM, and 25 μM) was simultaneously added and coincubated with anti-α_v or anti-β_3 antibody. Panels A−C: images of cells treated with 5 μM **DC-1**, 5 μM **DC-1** with anti-α_v antibody, or 5 μM **DC-1** with anti-β_3 antibody. Panels D−F: images of cells treated with 10 μM **DC-1**, 10 μM **DC-1** with anti-α_v antibody, or 10 μM **DC-1** with anti-β_3 antibody. Panels G−I: images of cells treated with 25 μM **DC-1**, 25 μM **DC-1** with anti-α_v antibody, or 25 μM **DC-1** with anti-β_3 antibody, respectively. Scale bars: 20 μm.

a concentration of 10 μg/mL. As illustrated in Figure 5B−C and SI Figure S7, rows B−C, at 5 μM concentration of **DC-1**, very few cells coincubated with anti-α_v or anti-β_3 antibodies show any **DC-1** binding and uptake. After the concentration of **DC-1** was increased to 10 μM, the amount of cells with internalized compound increased to ∼50% of the total number (Figure 5E,F and SI Figure S7, rows E,F) as compared to the control (Figure 5D and SI Figure S7, row D). Finally, at 25 μM concentration of **DC-1** cells showed fluorescent signal indicative of the compound competing with the antibody binding (Figure 5G−I and SI Figure S7, rows G−I). Based on this competition assay, we estimated an in vitro EC$_{50}$ for **DC-1** as ∼10 μM.

The data presented in Figures 4 and 5 and SI Figures S5 and S7 underscore the fact that while blocking the $\alpha_v\beta_3$ integrins by preincubating the cells with antibodies almost totally suppresses the binding and uptake of **DC-1**, a simultaneous addition of **DC-1** and antibodies causes **DC-1** to compete with binding of antibodies to $\alpha_v\beta_3$ integrins if **DC-1** is present at higher concentration.

To ascertain that **DC-1** and **DC-2** have low cytotoxicity in the absence of epithermal neutrons, we measured the rate of apoptosis by flow cytometry. In these experiments, WM115 cells were treated with either annexin V-PE (to detect an early apoptosis), or 7-AAD, a late apoptosis marker. The populations of the cells that spontaneously underwent early or late apoptosis (without treatment with **DC-1**) were determined first (SI Figures S4D and S4G). They were subsequently subtracted from the total populations of the apoptotic cells for the each group treated with **DC-1** (SI Figure S4E,F, and Figure S4H,I). We observed an increase in the rate of early apoptosis by 14%, for **DC-1**, and 4%, for **DC-2**. The rate of the late apoptosis increased by 13%, for **DC-1**, and by 1%, for **DC-2** (standard deviations for this type of assay are 1−1.5%; see SI Figure S4). This suggests that in the absence of high flux of epithermal neutrons the nontargeted agent **DC-2** is essentially noncytotoxic and targeted agent **DC-1** induces apoptosis at a very low rate.

In Vivo Imaging of Solid Tumor Targeting and Ex Vivo Biodistribution Study of DC-1. To assess tumor targeting ability of **DC-1** in vivo, the T-cell deficient nude mice were subcutaneously engrafted with WM115 cells, as described in the Experimental Section, and subsequently developed tumors with the mean volume of ca. 350 mm^3. We analyzed the extent of tumor targeting by **DC-1** relative to its accumulation in several vital organs. Remarkably, the emission of our cyanine dye was detectable in a broad range of wavelengths, reaching well into the red and near-IR regions and making possible imaging of its accumulation within the tumor and internal organs by the small animal imager without any modifications. The broad emission spectrum of the dye provided an opportunity to use several different excitation and emission wavelength for in vivo imaging. Three excitation wavelengths (λ_{ex} = 465, 500, and 535 nm) gave satisfactory signal in live animals at λ_{em} = 600−620 nm. In this experiment, **DC-1** at a dose of 5 mg/kg was injected into the mice via a lateral tail vein. Fluorescence images obtained with an excitation at 535 nm and emission was observed at 620 nm at specified time points (Figure 6A) have shown the best signal to noise ratio. Interestingly, **DC-1** shows localization in the tumor already 30 min after injection with the maximum signal intensity being observed after 2 h. Furthermore, **DC-1** showed retention in tumors with its fluorescence signal readily detectable in the tumor even after 7
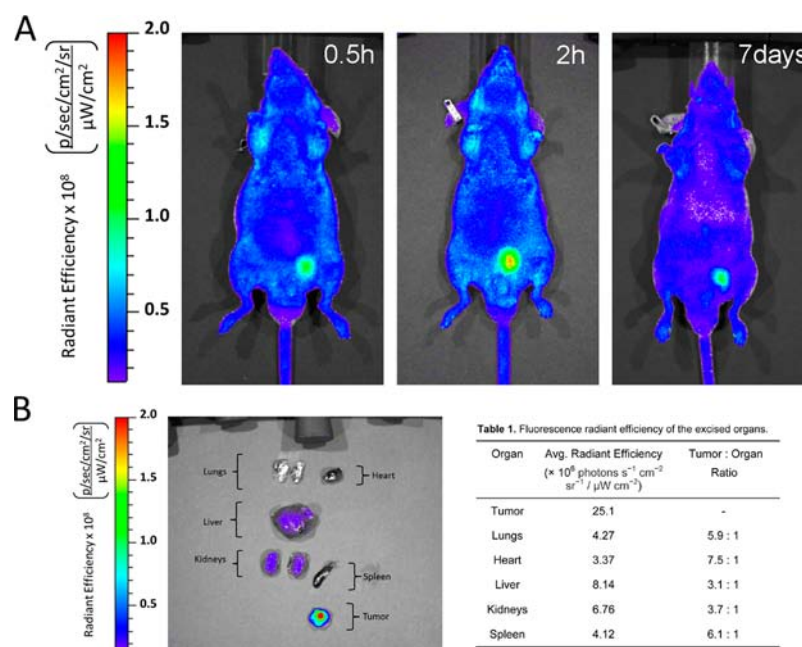
Figure 6. Tumor uptake and biodistribution of **DC-1** in vivo. (A) Representative fluorescence images acquired at three indicated time points after injection of **DC-1**. (B) Image of organs shows fluorescent signals from the tumor, lungs, heart, liver, kidneys, and spleen in the animal dissected 2 h after the injection.

days. We also performed a simple biodistribution study, where mice were injected via a lateral tail vein with 5 mg/kg dose of **DC-1** and after 2 h the animal was sacrificed and the vital organs were collected. Imaging showed a consistently higher degree of accumulation of **DC-1** in the tumor as compared to the other vital organs: lungs, heart, liver, kidneys, and spleen (Figure 6B and Table 1). The dissected organs could also be imaged at $\lambda_{ex} = 500/\lambda_{em} = 560$ nm (SI Figure S8), due to the fact that the excitation light with the lower wavelength is no longer absorbed by the animal's skin and underlying tissues. We observed the greatest accumulation of the conjugate in the tumor, as expected. The liver and kidneys also showed an accumulation of **DC-1**, 3.1- and 3.7-fold lower than the tumor. The readily detectable signal of the conjugate in the kidneys suggests them as the likely primary organs through which the excretion of the conjugate could occur. The achieved tumor-to-organ ratio of the accumulated agent was greater than 3:1 in all imaged organs (Table 1) with the rest of the organs and body showing even lower levels of the signal. These results underscore the potential of **DC-1** for BNCT. Further measurements of plasma half-life, RES uptake, and other pharmacokinetic data are underway and will be reported in due course.

In order to determine the uptake and localization of our agents in vivo in greater detail, we used intravital microscopy (IVM) imaging of murine mammary adenocarcinoma in nude mice. This method offers a remarkably detailed view of the tumor development, allowing dynamic, high resolution, in vivo imaging of molecular, and cellular events. Individual tissue cells can be imaged by standard light and fluorescence microscopy such that many cellular events (e.g., cell migration, mitosis, pyknosis, and apoptosis) and the growth and connectivity of blood vessels can be readily quantified. IVM is especially powerful at imaging dynamic changes, such as rapid flux of fluorescent probes across the endothelial cell barrier, tumor

uptake of fluorescent probes, changes in blood flow, and tumor responses to therapeutic agents.

In our IVM experiments, a titanium frame was placed onto the dorsal skinfold of nude mice to sandwich the extended double layer of skin, and the skin was carefully removed to expose the underlying muscle and subcutaneous tissue, which was covered with another titanium frame with a glass coverslip to form the window chamber. Tumor spheroids that consisted of N202 cells (murine mammary carcinoma) were then implanted into the tissue and allowed to vascularize and grow into a tumor.[27] After the tumor formation, the conjugate **DC-1** or the nontargeted compound **DC-2** was injected via the tail vein at a dose of 2 mg/kg. The fluorescence images were then recorded on specified days at the emission wavelength of the dye incorporated into the constructs.

The IVM images show the accumulation of **DC-1** in the tumor, as shown by the signal on Day 1 and its retention within the tumor for 7 days (Figure 7). Interestingly, the signal inside the tumor blood vessels was lower and contrasted with the signal concentrating within the tumor interstitium even after the first day past injection. This shows that **DC-1** moved across the leaky vascular wall of the subcutaneous tumors and
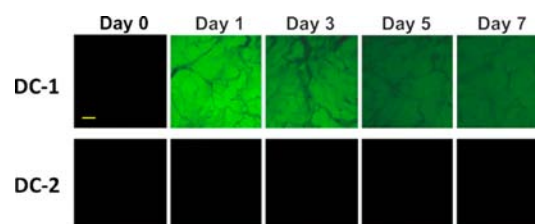

Figure 7. IVM images showing the uptake and retention of **DC-1** in mouse subcutaneous tumor xenografts after injection at 2 mg/kg on Day 0. A substantial amount of **DC-1** is accumulated in the tumor on Day 1 and is detectable for 7 days. The black shadows in all images are tumor blood vessels. Scale bar: 100 μm.

accumulated inside the tumors after being injected. The nontargeted **DC-2** injected at the same dose did not show any detectable signal within the tumors.

CONCLUSIONS

We designed, synthesized, and performed in vitro and in vivo assessment of tumor targeting theranostic agent **DC-1**. This multifunctional conjugate combines diagnostic (visible-light imaging) and therapeutic (BNCT) modalities with tumor targeting through its ability to bind $\alpha_v\beta_3$ integrins. As illustrated by our competition experiments using anti-α_v and anti-β_3 antibodies, cellular uptake of **DC-1** is dose-dependent and can be significantly inhibited through a selective blockade of the $\alpha_v\beta_3$ receptors. In our murine subcutaneous tumor xenografts, **DC-1** rapidly and specifically accumulated in the solid tumors, as illustrated by live animal imaging and ex vivo analysis of the compound biodistribution. Imaging experiments using subcutaneous models showed rapid uptake, tumor to organs ratio greater than 3:1, and a significant retention of **DC-1** in the tumors for up to 7 days, providing a broad time window for diagnostic and therapeutic use of the conjugate.

Targeted dendritic wedges provide an attractive platform to transport diagnostic and therapeutic modalities into tumors. Future efforts will focus on biodistribution, pharmacokinetic and pharmacodynamics analysis, and in vivo testing of the therapeutic efficacy of this promising delivery platform in a range of tumor models. It is also of particular interest to test the targeting strategy described herein in patient-derived primary tumors where physical barriers, such as microvascular wall, could pose challenges for the delivery of therapeutic agents from the circulating blood across the vascular endothelial barrier.

EXPERIMENTAL PROCEDURES

General. All reagents and solvents were obtained from commercial sources and were used as received unless otherwise stated. Dry THF was obtained by distillation with sodium and benzophenone. Dry CH_2Cl_2 was freshly distilled with calcium hydride. All reactions involving moisture-sensitive reagents were conducted under argon atmosphere with anhydrous solvents and flame-dried glassware. Hygroscopic liquids were transferred via a syringe and were introduced into reaction vessels through rubber septa. Reaction product solutions were concentrated using a rotary evaporator at 30−150 mmHg. Column chromatography was performed on silica gel (230−400 mesh) using reagent grade solvents as eluents. Analytical thin-layer chromatography (TLC) was performed on glass-backed, pre-coated plates (0.25 mm, silica gel 60, F-254, EM Science). Preparatory HPLC purifications were carried out on C_8 reverse phase preparative column (Alltech/Grace Davison) using the flow rate of either 4 or 5 mL/min. In all cases, various gradients of acetonitrile in 0.1% aqueous trifluoroacetic acid (TFA) were used as eluents. Water (18 MΩ) was obtained from a Millipore Milli-Q water purification system, and all buffers were filtered through 0.2 μm nylon filter immediately before use. Nuclear magnetic resonance (NMR) spectra were obtained on Varian 400 or Bruker 500 MHz instruments in the indicated solvents. The peak positions are reported with chemical shifts (δ) in parts per million (ppm) downfield from the signal for tetramethylsilane (0 ppm) and referenced to the signal resulting from the incomplete deuteration of a solvent used in the experiment (CDCl$_3$: 7.26 ppm, or the center line of

the multiplet of DMSO-d_6: 2.50 ppm). Carbon-13 chemical shifts are reported as δ values in ppm and referenced to the cabon-13 signal of a solvent used in the experiment (CDCl$_3$: 77.0 ppm, or the center line of the multiplet DMSO-d_6: 39.51 ppm). The following abbreviations are used: singlet (s), doublet (d), triplet (t), doublet of doublets (dd), multiplet (m). UV−vis absorption spectra were measured on Beckman DU-800 spectrophotometer. Fluorescence emission spectra were measured using Horiba Fluorolog spectrofluorometer. Mass spectra were obtained with Thermo Finnigan LCQ or Agilent 6200 Series Accurate-Mass Time-of-Flight (TOF) LCMS instruments, School of Pharmacy, University of Southern California and Bruker IonSpec 4.7T ESI FT-ICR mass spectrometer at the University of Arizona, Tucson. Compound **3** was prepared by a procedure analogous to that described in the literature.[24]

Conjugate 5 (Scheme 1). Neat TFA (3 mL) was added to a solution of **3** (30 mg, 0.047 mmol) in CH_2Cl_2 (3 mL). The resulting solution was stirred for 30 min at ambient temperature. Then, the solvent was removed under reduced pressure, and the resulting deprotected amine was dissolved in a mixture of DMF (1 mL) and DIEA (42 μL, 0.234 mmol). Separately, N_ε-Cbz-N_α-Boc-L-lysine (**4**, 18 mg, 0.047 mmol) was dissolved in DMF (1 mL), followed by the addition of HBTU (30 mg, 0.072 mmol) and DIEA (42 μL, 0.234 mmol). After stirring for 10 min, this mixture was added dropwise to the deprotected amine and the reaction mixture was stirred for 2 h. The solvent was removed under reduced pressure and the residue was purified by column chromatography (silica gel, CH_2Cl_2/MeOH (95:5)) to yield **5** (40 mg, 95%) as a colorless, glass-like solid. ^{1}H NMR (600 MHz, CDCl$_3$) δ 8.85 (1H, br s), 8.33 (2H, br s), 7.64 (2H, d, J = 5 Hz), 7.40−7.25 (10H, m), 6.98 (1H, br s), 6.88 (2H, d, J = 5 Hz), 6.76−6.65 (2H, m), 5.42 (1H, br d), 5.21 (2H, s), 5.06 (3H, s), 4.49 (1H, br s), 4.20−4.00 (3H, m), 3.92 (3H, br s), 3.85−3.67 (2H, m), 3.50 (1H, br s), 3.23−3.20 (4H, m), 1.73 (1H, br s), 1.58 (1H, br s), 1.42 (9H, s), 1.25 (2H, br s). HRMS (ESI) calculated for $C_{44}H_{57}N_8O_{11}S$ [M + H]$^+$: 905.3868, found: 905.3864.

N,N-Di-Boc-Dipropylenetriamine Glutarate 6. N,N-Di-boc-dipropylenetriamine[25] (125 mg, 0.377 mmol) and glutaric anhydride (130 mg, 1.14 mmol) were dissolved in CHCl$_3$ (3 mL). DIEA (200 μL, 1.14 mmol) was added, and the mixture was heated to reflux. After 3 h, the reaction mixture was cooled down to ambient temperature and the solvent was removed under reduced pressure. The residue was purified by column chromatography (silica gel, CH_2Cl_2/MeOH (95:5)) to yield **6** (110 mg, 65%) as a colorless, viscous oil. ^{1}H NMR (600 MHz, CDCl$_3$) δ 5.30 (1H, br s), 4.85 (1H, br s), 3.39−3.38 (2H, m), 3.29−3.27 (2H, m), 3.13 (2H, br s), 3.07−3.04 (2H, m), 2.42−2.40 (4H, m), 1.98−1.94 (2H, m), 1.76 (2H, br s), 1.68−1.64 (2H, m), 1.43 (18H, s). ^{13}C NMR (125 MHz, CDCl$_3$) δ 176.5, 172.8, 156.2, 79.70, 79.04, 45.42, 42.75, 38.08, 37.38, 33.26, 31.79, 29.78, 28.46, 28.39, 27.99, 20.69. HRMS (ESI) calculated for $C_{21}H_{40}N_3O_7$ [M + H]$^+$: 446.2866, found: 446.2861.

Conjugate 7. Neat TFA (3 mL) was added to a solution of **5** (30 mg, 0.033 mmol) in CH_2Cl_2 (3 mL). The resulting solution was stirred for 30 min at ambient temperature. Then, the solvent was removed under reduced pressure and the resulting deprotected amine was dissolved in a mixture of DMF (1 mL) and DIEA (30 μL, 0.165 mmol). Separately, **6** (15 mg, 0.033 mmol) was dissolved in DMF (1 mL) followed by the addition of HBTU (19 mg, 0.050 mmol) and DIEA (30 μL,

0.165 mmol). After stirring for 10 min, this reaction mixture was added dropwise to the solution of the deprotected amine. The resulting mixture was stirred for 2 h. Solvent was removed under reduced pressure, and the residue was purified by column chromatography (silica gel, CH_2Cl_2/MeOH (93:7)) to yield **7** (40 mg, 98%) as a colorless, glass-like solid. ^{1}H NMR (600 MHz, $CDCl_3$) δ 8.75 (1H, br s), 8.35 (2H, br s), 8.08 (1H, br s), 7.72−7.60 (2H, m), 7.51−7.14 (13H, m), 6.86 (2H, d, J = 5 Hz), 6.67 (1H, br s), 5.50−5.00 (5H, m), 4.52 (1H, br d), 4.32−3.70 (5H, m), 3.69 (1H, br d), 3.55−2.70 (16H, m), 2.40−2.20 (2H, m), 2.19−2.00 (3H, m), 1.78−1.60 (4H, m), 1.55−1.39 (23H, m). HRMS (ESI) calculated for $C_{60}H_{86}N_{11}O_{15}S$ $[M + H]^+$: 1232.6026, found: 1232.6020.

Synthesis of DC-1. Neat TFA (2 mL) was added to a solution of **7** (18 mg, 0.015 mmol) in CH_2Cl_2 (2 mL). The resulting solution was stirred for 30 min at ambient temperature. Then, the solvent was removed under reduced pressure and the resulting deprotected amine was dissolved in a mixture of DMF (0.5 mL) and DIEA (7 µL, 0.045 mmol). Separately, the carborane dendritic wedge **8** (21 mg, 0.030 mmol) was dissolved in DMF (0.5 mL), followed by the addition of HBTU (14 mg, 0.038 mmol) and DIEA (7 µL, 0.045 mmol). After stirring for 10 min, the resulting mixture was added dropwise to the solution of the deprotected amine and the mixture was stirred for 2 h. Once the reaction was complete, solvent was removed under reduced pressure and the residue was dissolved in EtOH (2 mL), followed by the addition of AcOH (25 µL) and Pd black (10 mg). The vial was purged with H_2, and the solution was stirred under an H_2 atmosphere for 3 h. The solids were filtered off, and the filtrate was concentrated under reduced pressure to obtain compound **9**, which was dissolved in DMF (1 mL), followed by the addition of DIEA (7 µL, 0.042 mmol) and dye **10** (5.0 mg, 0.016 mmol). The reaction was monitored by analytical HPLC. Upon completion, the mixture was diluted with MeOH (2 mL) and purified by preparative HPLC to yield **DC-1** (9 mg, 25%) as a viscous orange oil. ^{1}H NMR (600 MHz, CD_3OD) δ 7.84−7.81 (2H, m), 7.74 (1H, d, J = 8 Hz), 7.52−7.50 (1H, m), 7.46 (1H, d, J = 8 Hz), 7.30−7.28 (1H, m), 7.23 (2H, s), 7.03−6.99 (2H, m), 4.52 (6H, br s), 4.39−4.32 (2H, m), 4.23−4.15 (5H, m), 4.09 (6H, s), 3.94−3.90 (16H, m), 3.89−3.84 (2H, m), 3.72−3.54 (11H, m), 3.50−3.44 (12H, m), 3.40−3.35 (12H, m), 3.21 (3H, t, J = 5 Hz), 3.16 (3H, t, J = 5 Hz), 2.71−1.65 (82H, m). ^{11}B NMR (160 MHz, CD_3OD) δ −1.91, −4.01, −8.45, −10.60, −11.95. UV−vis (MeOH): 445, 249, and 203 nm. HRMS (ESI) calculated for $C_{87}H_{175}B_{60}N_{12}O_{21}S_2$ $[M+2H]^{2+}$: 1219.9263, found: 1219.9338; FTICR MS: isotope pattern is consistent with the expected composition (see SI Figures S20 and S21).

***N,N*-Di-Boc-Dipropylenetriamine 6-Aminohexanoic Acid 11 (SI Scheme S1).** Cbz-6-aminohexanoic acid (100 mg, 0.377 mmol) was dissolved in a mixture of DMF (2 mL), DIEA (134 µL, 0.754 mmol), and HBTU (143 mg, 0.377 mmol), and the mixture was stirred for 10 min. Then, *N,N*-di-boc-dipropylenetriamine[25] (125 mg, 0.377 mmol) was added in one installment and the resulting mixture was stirred for 1 h. The solvent was then removed under reduced pressure and the residue was purified by column chromatography (silica gel, CH_2Cl_2/MeOH (93:7)) to yield **11** (142 mg, 65%) as a colorless, viscous oil. ^{1}H NMR (600 MHz, $CDCl_3$) δ 7.35−7.29 (5H, m), 5.33 (1H, br s), 5.09 (2H, s), 4.93 (1H, br s), 4.81 (1H, br s), 3.40−3.38 (2H, m), 3.37−3.02 (8H, m), 2.30 (2H, t, J = 7 Hz), 1.78−1.35 (28H, m). ^{13}C NMR (125 MHz,

$CDCl_3$) δ 173.1, 156.4, 156.1, 156.0, 136.6, 128.4, 128.0, 79.51, 78.88, 66.56, 45.33, 42.49, 40.77, 38.13, 37.27, 32.73, 29.90, 29.67, 28.47, 28.4, 28.00, 26.36, 24.88. HRMS (ESI) calculated for $C_{30}H_{51}N_4O_7$ $[M + H]^+$: 579.3758, found: 579.3759.

Synthesis of DC-2. Pd black (10 mg) was added to a solution of **11** (15 mg, 0.026 mmol) in MeOH (2 mL), and the solution was purged with H_2 and stirred under H_2 atmosphere at ambient pressure for 3 h. The solids were filtered off, and the filtrate was concentrated under reduced pressure. The residue was dissolved in DMF (1 mL), and DIEA (8 µL, 0.052 mmol) and cyan 39 **10** (16 mg, 0.052 mmol) were added. The resulting mixture was stirred at ambient temperature for 1 h, the solvent was removed under reduced pressure, and the residue **12** was dissolved in a mixture of CH_2Cl_2 (2 mL) and TFA (2 mL). The resulting solution was stirred for 30 min at ambient temperature. The solvent was removed under reduced pressure and the resulting deprotected amine was dissolved in a mixture of DMF (0.5 mL) and DIEA (23 µL, 0.13 mmol). Separately, the carborane dendritic wedge **8** (37 mg, 0.052 mmol) was dissolved in a mixture of DMF (1 mL), HBTU (20 mg, 0.052 mmol), and DIEA (23 µL, 0.13 mmol). The mixture was stirred for 10 min and added dropwise to the solution of the deprotected amine. The combined mixture was stirred for 2 h. Solvent was removed under reduced pressure, and the residue was dissolved in MeOH (5 mL) and purified by semiprep HPLC to yield **DC-2** (10 mg, 21%) as viscous orange oil. ^{1}H NMR (600 MHz, CD_3OD) δ 7.75 (1H, d, J = 8 Hz), 7.52−7.43 (2H, m), 7.33−7.25 (2H, m), 7.23 (2H, s), 4.27−4.20 (2H, m), 4.10 (4H, s), 3.96−3.81 (14H, m), 3.70 (3H, s), 3.52−3.33 (20H, m), 3.22−3.11 (8H, m), 2.72−1.30 (82H). ^{11}B NMR (160 MHz, CD_3OD) δ −1.91, −3.85, −8.44, −10.62, −11.94. UV−vis (MeOH): 442, 266, 227, and 202 nm. HRMS (ESI) calculated for $C_{64}H_{144}B_{60}N_5O_{13}S$ $[M+2H]^{2+}$: 935.8213, found: 935.8208.

Quantum Yield Measurements. To determine quantum yields for **DC-1** and **DC-2**, 20 µM stock solutions of both compounds were prepared in nonviscous (neat DMSO) and viscous (9/1 v/v glycerol/DMSO) solvents. The stock solutions were prepared using the respective solvents in order to achieve the absorption of 0.1 at 450 nm. These solutions were subjected to further serial dilutions, and the absorption spectra of the diluted solutions were measured. Fluorescence emission spectra of the same solutions were measured at λ_{ex} = 450 nm. The integrated fluorescence intensities were calculated from the fluorescnce emission spectra by measuring the area under the curve. The absorption of each sample at 450 nm was plotted against the integrated fluorescence intensity for that sample (SI Figure S3). A simple linear regression was obtained from the data and the gradient was calculated. Using the above-mentioned procedure, a reference plot of absorption at 450 nm vs the integrated fluorescnce intensity was also made and the gradient was calculated for the known standard (5-carboxyfluorescein in 0.1 M NaOH, quantum yield 95%). The formula used to calculate the quantum yields of **DC-1** and **DC-2** is shown in the SI Figure S3.

Cell Lines. Human breast carcinoma (MCF7) and human melanoma (WM115) cell were obtained from ATCC (accession numbers HTB-22 and CRL-1675). Murine mammary adenocarcinoma N202 was a gift from Joseph Lustgarten, Mayo Clinic, Scottsdale, AZ.

Cell Culture. MCF7 cells were maintained in RPMI 1640 media (Sigma) supplemented with 10% fetal bovine serum (Irvine Scientific), penicillin (50 U/mL), and streptomycin (50

μg/mL). WM115 cells were grown in α-MEM (Sigma) supplemented with 10% fetal bovine serum, penicillin (50 U/mL), and streptomycin (50 μg/mL). MCF7 and WM115 were passaged after they became 90% confluent using 1% Trypsin for MCF7 cells and 1× Accutase (Sigma) for WM115 cells. All cells were incubated at 37 °C in a humidified atmosphere with 5% CO_2. N202 cells were maintained in DMEM High Glucose supplemented with L-glutamine (2 mM), penicillin (100 U/mL), streptomycin (100 U/mL), sodium pyruvate (1 mM) (Invitrogen, Carlsbad, CA), and 10% heat inactivated FBS (Omega Scientific, Tarzana, CA). All cells were maintained at 37 °C in a humidified atmosphere with 5% CO_2. Cell growth and morphology were monitored by phase-contrast microscopy.

Flow Cytometry. WM115 cells were plated in a 25 mL cell culture flask. After 48 h cells were harvested with Accutase (Sigma) and resuspended in PBS at a concentration of 1×10^6 cells/mL. Next, 100 μL of cell suspension was incubated at 37 °C for 4 h with **DC-1** (25 μM) in α-MEM medium with 1% DMSO in a culture tube. Cells were centrifuged at 500×g and washed with ice-cold PBS. To the cells was added 5 μL of Annexin V-PE or 5 μL of 7-AAD for 15 min at room temperature in the dark followed by the addition of 400 μL of binding buffer. For control experiments, cells were incubated with Annexin V-PE or 7-AAD only in α-MEM medium with 1% DMSO. After incubation, the cells were analyzed by a BD LSR II flow cytometer and fluorescence emitted was collected in three optical channels as indicated in Table S1.

Confocal Microscopy. In our laser-scanning confocal microscopy (LSCM) experiments, Mat Tek 35-mm-diameter dishes with 14 mm glass bottom were used. A general method for confocal microscopy consisted of plating 30 000 cells, MCF7 or WM115 in glass bottom dish with 300 μL RPMI medium and α-MEM medium for MCF7 and WM115 cell lines, respectively. Both media were supplemented with 10% fetal bovine serum. After 24 h the dishes with cells were treated with compounds **DC-1** and **DC-2** at desired concentration in their media supplemented with 10% fetal bovine serum and DMSO at 1% v/v. The cells were incubated with compounds for desired length of time. In general, incubation time given to cells treated with **DC-1** and **DC-2** was 14 h at 37 °C at 5% CO_2. For 4 °C experiments, a 2 h incubation was performed in a plastic wrap to avoid evaporation of the cell culture media. Zeiss LSM510 META Confocal Imaging System equipped with oil-immersion objectives for 40× or 63× magnification was used. Argon 488 nm laser was used for imaging with emission filters of BP 500−550 IR.

Blocking Experiments with Antibodies. For antibody blocking experiments, WM115 cells were harvested with Accutase (Sigma) and plated on Mat Tek 35-mm-diameter dishes with 14 mm glass bottom. After 48 h of incubation of the plated cells, they were treated with either anti-α_v (10 μg/mL) or anti-β_3 (10 μg/mL) antibodies (Millipore) in α-MEM medium with 1% DMSO for 1 h. Next, **DC-1** or **DC-2** at a desired concentration was added to the medium and the cells were coincubated with **DC-1** or **DC-2** and the antibodies for 2 h. Cells were washed with cold PBS and treated with secondary antibody for 0.5 h at room temperature in the dark followed by two washes with ice-cold PBS. In order to detect anti-α_v antibody, cells were washed with ice-cold PBS and incubated with the secondary antibody, Alexa Fluor 594−goat anti-mouse IgG (Invitrogen) at a 10 μg/mL concentration for 30 min, then washed with ice-cold PBS immediately before imaging.

Similarly, Alexa Fluor 350 goat anti-mouse IgM (μ chain, 10 μg/mL, Invitrogen) has been used for detection of anti-β_3 primary antibody.

For antibody competition experiments, WM115 cells were harvested with Accutase (Sigma) and plated on Mat Tek 35-mm-diameter dishes with 14 mm glass bottom. After 48 h of incubation of the plated cells, they were coincubated with desired concentration of **DC-1** or **DC-2** and with either anti-α_v (10 μg/mL) or anti-β_3 (10 μg/mL) antibodies (Millipore) in α-MEM medium with 1% DMSO for 3 h. Cells were washed with cold PBS and imaged.

Zeiss LSM510 META confocal microscope equipped with oil-immersion objectives for 40× or 63× magnification was used. Argon 488 nm laser was used for imaging **DC-1** and **DC-2**, 543 nm laser was used for imaging Alexa Fluor 594 secondary antibody, and 790 nm laser was used for two photon excitation of Alexa Fluor 350 secondary antibody. Emission filters used were BP 500−550 IR, BP 565−615 IR, and Track ChS1:362−704 for green, red, and blue channels, respectively.

Animal Use. Animal experiments were done in accordance with federal guidelines following review and approval by the Proteogenomics Research Institute for Systems Medicine Institutional Animal Care and Use Committee (PRISM IACUC) and University of Southern California IACUC. Athymic nude mice were 8−9 weeks old and purchased from Harlan or Taconic.

Tumor Models. The athymic nude mice were anesthetized (3% isoflurane) and WM115 cells, 5 million cells per site in 50 μL αMEM medium and 50 μL BD Matrigel, were injected subcutaneously into the lower dorsal right flank in five mice. Mice developed medium-sized (350 mm^3) subcutaneous tumor on the ventral left side of the mice after 4 weeks of injection.

Imaging of Live Mice. The mice with a ventral side subcutaneous tumor (350 mm^3 size) were anesthetized (3% isoflurane). A solution of **DC-1** was injected intravenously via lateral tail vein at a dose of 5 mg/kg. Xenogen IVIS 200 instrument was used for the imaging. Images were taken after an interval of 30 min, 2 h, and 7 days after injecting **DC-1** at excitation wavelength of 535 nm and measuring emission at 620 nm. For the biodistribution study, **DC-1** was injected at a dose of 5 mg/kg via tail vein, the animal was euthanized after 2 h, and dissection was performed to collect the organs. The collected organs were immediately imaged at λ_{ex} = 500 nm/λ_{em} = 560 nm and at λ_{ex} = 535 nm/λ_{em} = 620 nm.

Intravital Microscopy Imaging. We used a classical IVM tumor model with minor modifications.[26] The mice, athymic nude mice (25−30 g body weight), were anesthetized (7.3 mg ketamine hydrochloride and 2.3 mg xylazine per 100 g body weight, intraperitoneal injection) and placed on a heating pad. A titanium frame was placed onto the dorsal skinfold of mice to sandwich the extended double layer of skin. A 15-mm-diameter full-thickness circular layer of skin was then excised. The superficial fascia on top of the remaining skin is carefully removed to expose the underlying muscle and subcutaneous tissue which is then covered with another titanium frame with a glass coverslip to form the window chamber. After a recovery period of 1−2 days, the animals were prepared for the procedure of implanting of tumor spheroids.

Tumor spheroids were formed by plating 50 000 N202 cells onto 1% agar-coated 96-well non-tissue culture treated flat bottom dishes (20 μL cells in 100 μL medium) and centrifuging 4 times at 2000 rpm for 15 min, rotating the dish after every centrifugation. The cells were incubated an

additional 3−7 days (depending on cell type) at 37 °C in 5% CO_2 in air to form tight tumor spheroids. The spheroids were implanted directly onto the dorsal skin in the window chamber alone. Tumors were allowed to vascularize over 10−14 days before the injection of 1 mg/kg of either **DC-1** or **DC-2** on Day 0.

Tumor Growth. Tumors were imaged via intravital fluorescence microscopy, as described in the literature.[27] The amount of integrin ligand retention in tumors was analyzed from the recorded grayscale 0-to-256 levels of gray images using Image-Pro Plus (Media Cybernetics, Bethesda, MD). Intravital fluorescence microscopy was done on days 1, 3, 5, and 7 to analyze the amount of **DC-1** and **DC-2** present in the tumors.

■ ASSOCIATED CONTENT

ⓢ Supporting Information

Synthesis, characterization, absorption, fluorescence excitation spectra for **DC-2**, in vitro experiments. This material is available free of charge via the Internet at http://pubs.acs.org.

■ AUTHOR INFORMATION

Corresponding Authors
*E-mail: i.zharov@utah.edu.
*E-mail: bogdan@usc.edu.

Notes
The authors declare no competing financial interest.

■ ACKNOWLEDGMENTS

■ REFERENCES

(1) Kolonin, M. G. (2009) Tissue-Specific Targeting Based on Markers Expressed Outside Endothelial Cells, In *Tissue-Specific Vascular Endothelial Signals and Vector Targeting, Part A* (Pasqualini, R., and Arap, W., Eds.) pp 61−102, San Diego, Elsevier.

(2) Al-Jamal, W. T., and Kostarelos, K. (2011) Liposomes: from a clinically established drug delivery system to a nanoparticle platform for theranostic nanomedicine. *Acc. Chem. Res. 44*, 1094−1104.

(3) Luk, B. T., Fang, R. H., and Zhang, L. F. (2012) Lipid- and polymer-based nanostructures for cancer theranostics. *Theranostics 2*, 1117−1126.

(4) Ostrowski, A. D., Lin, B. F., Tirrell, M. V., and Ford, P. C. (2012) Liposome encapsulation of a photochemical NO precursor for controlled nitric oxide release and simultaneous fluorescence imaging. *Mol. Pharmaceutics 9*, 2950−2955.

(5) Petersen, A. L., Hansen, A. E., Gabizon, A., and Andresen, T. L. (2012) Liposome imaging agents in personalized medicine. *Adv. Drug Delivery Rev. 64*, 1417−1435.

(6) Soenen, S. J., Vande Velde, G., Ketkar-Atre, A., Himmelreich, U., and De Cuyper, M. (2011) Magnetoliposomes as magnetic resonance imaging contrast agents. *Wiley Interdiscip. Rev.-Nanomed. Nanobiotechnol. 3*, 197−211.

(7) Lo, S. T., Kumar, A., Hsieh, J. T., and Sun, X. K. (2013) Dendrimer nanoscaffolds for potential theranostics of prostate cancer with a focus on radiochemistry. *Mol. Pharmaceutics 10*, 793−812.

(8) Oliveira, J. M., Salgado, A. J., Sousa, N., Mano, J. F., and Reis, R. L. (2010) Dendrimers and derivatives as a potential therapeutic tool in regenerative medicine strategies-A review. *Prog. Polym. Sci. 35*, 1163−1194.

(9) Lammers, T., Subr, V., Ulbrich, K., Hennink, W. E., Storm, G., and Kiessling, F. (2010) Polymeric nanomedicines for image-guided drug delivery and tumor-targeted combination therapy. *Nano Today 5*, 197−212.

(10) Lollo, G., Rivera-Rodriguez, G., Torres, D., and Alonso, M. J. (2011) Oncologic nanotherapies: current applications and future perspectives. *An. R. Acad. Nac. Farm. 77*, 76−98.

(11) Nystrom, A. M., and Wooley, K. L. (2011) The importance of chemistry in creating well-defined nanoscopic embedded therapeutics: devices capable of the dual functions of imaging and therapy. *Acc. Chem. Res. 44*, 969−978.

(12) Ofek, P., Miller, K., Eldar-Boock, A., Polyak, D., Segal, E., and Satchi-Fainaro, R. (2010) Rational design of multifunctional polymer therapeutics for cancer theranostics. *Isr. J. Chem. 50*, 185−203.

(13) Puri, A., and Blumenthal, R. (2011) Polymeric lipid assemblies as novel theranostic tools. *Acc. Chem. Res. 44*, 1071−1079.

(14) Ambrogio, M. W., Thomas, C. R., Zhao, Y. L., Zink, J. I., and Stoddartt, J. F. (2011) Mechanized silica nanoparticles: a new frontier in theranostic nanomedicine. *Acc. Chem. Res. 44*, 903−913.

(15) Arosio, D., Casagrande, C., and Manzoni, L. (2012) Integrin-mediated drug delivery in cancer and cardiovascular diseases with peptide-functionalized nanoparticles. *Curr. Med. Chem. 19*, 3128−3151.

(16) Debbage, P., and Jaschke, W. (2008) Molecular imaging with nanoparticles: giant roles for dwarf actors. *Histochem. Cell Biol. 130*, 845−875.

(17) Iyer, A. K., He, J., and Amiji, M. M. (2012) Image-guided nanosystems for targeted delivery in cancer therapy. *Curr. Med. Chem. 19*, 3230−3240.

(18) Janib, S. M., Moses, A. S., and MacKay, J. A. (2010) Imaging and drug delivery using theranostic nanoparticles. *Adv. Drug Delivery Rev. 62*, 1052−1063.

(19) Kunjachan, S., Jayapaul, J., Mertens, M. E., Storm, G., Kiessling, F., and Lammers, T. (2012) Theranostic systems and strategies for monitoring nanomedicine-mediated drug targeting. *Curr. Pharm. Biotechnol. 13*, 609−622.

(20) Lammers, T., Aime, S., Hennink, W. E., Storm, G., and Kiessling, F. (2011) Theranostic nanomedicine. *Acc. Chem. Res. 44*, 1029−1038.

(21) Lammers, T., Kiessling, F., Hennink, W. E., and Storm, G. (2010) Nanotheranostics and image-guided drug delivery: current concepts and future directions. *Mol. Pharmaceutics 7*, 1899−1912.

(22) Lammers, T., Kiessling, F., Hennink, W. E., and Storm, G. (2012) Drug targeting to tumors: Principles, pitfalls and (pre-) clinical progress. *J. Controlled Release 161*, 175−187.

(23) Svenson, S. (2013) Theranostics: are we there yet? *Mol. Pharmaceutics 10*, 848−856.

(24) Duggan, M. E., Duong, L. T., Fisher, J. E., Hamill, T. G., Hoffman, W. F., Huff, J. R., Ihle, N. C., Leu, C. T., Nagy, R. M., Perkins, J. J., Rodan, S. B., Wesolowski, G., Whitman, D. B., Zartman, A. E., Rodan, G. A., and Hartman, G. D. (2000) Nonpeptide alpha(v)beta(3) antagonists. 1. Transformation of a potent, integrin-selective alpha(IIb)beta(3) antagonist into a potent alpha(v)beta(3) antagonist. *J. Med. Chem. 43*, 3736−3745.

(25) Ghatnekar, J., Haegerloef, M., Oredsson, S., Alm, K., Elmroth, S. K. C., and Persson, T. (2007) Construction of polyamine-modified uridine and adenosine derivatives-evaluation of DNA binding capacity and cytotoxicity in vitro. *Bioorg. Med. Chem. 15*, 7426−7433.

(26) Dubey, R., Levin, M. D., Szabo, L. Z., Laszlo, C. F., Kushal, S., Singh, J. B., Oh, P., Schnitzer, J. E., and Olenyuk, B. Z. (2013) Suppression of tumor growth by designed dimeric epidithiodiketopiperazine targeting hypoxia-inducible transcription factor complex. *J. Am. Chem. Soc. 135*, 4537−49.

(27) Oh, P., Borgstrom, P., Witkiewicz, H., Li, Y., Borgstrom, B. J., Chrastina, A., Iwata, K., Zinn, K. R., Baldwin, R., Testa, J. E., and Schnitzer, J. E. (2007) Live dynamic imaging of caveolae pumping targeted antibody rapidly and specifically across endothelium in the lung. *Nat. Biotechnol. 25*, 327−37.

(28) Hynes, R. O. (2002) Integrins: Bidirectional, allosteric signaling machines. *Cell 110*, 673−687.

(29) Gottschalk, K. E., and Kessler, H. (2002) The structures of Integrins and integrin-ligand complexes: Implications for drug design and signal transduction. *Angew. Chem., Int. Ed. 41*, 3767−3774.

(30) Brooks, P. C., Stromblad, S., Sanders, L. C., vonSchalscha, T. L., Aimes, R. T., StetlerStevenson, W. G., Quigley, J. P., and Cheresh, D. A. (1996) Localization of matrix metalloproteinase MMP-2 to the surface of invasive cells by interaction with integrin alpha v beta 3. *Cell 85*, 683−693.

(31) Eliceiri, B. P., and Cheresh, D. A. (1999) The role of alpha v integrins during angiogenesis: insights into potential mechanisms of action and clinical development. *J. Clin. Invest. 103*, 1227−1230.

(32) Hood, J. D., Bednarski, M., Frausto, R., Guccione, S., Reisfeld, R. A., Xiang, R., and Cheresh, D. A. (2002) Tumor regression by targeted gene delivery to the neovasculature. *Science 296*, 2404−2407.

(33) Hawthorne, M. F., and Maderna, A. (1999) Applications of radiolabeled boron clusters to the diagnosis and treatment of cancer. *Chem. Rev. 99*, 3421−3434.

(34) Soloway, A. H., Tjarks, W., Barnum, B. A., Rong, F. G., Barth, R. F., Codogni, I. M., and Wilson, J. G. (1998) The chemistry of neutron capture therapy. *Chem. Rev. 98*, 1515−1562.

(35) Barth, R. F., Coderre, J. A., Vicente, M. G. H., and Blue, T. E. (2005) Boron neutron capture therapy of cancer: Current status and future prospects. *Clin. Cancer Res. 11*, 3987−4002.

(36) Kankaanranta, L., Seppälä, T., Koivunoro, H., Saarilahti, K., Atula, T., Collan, J., Salli, E., Kortesniemi, M., Uusi-Simola, J., Välimäki, P., Mäkitie, A., Seppänen, M., Minn, H., Revitzer, H., Kouri, M., Kotiluoto, P., Seren, T., Auterinen, I., Savolainen, S., and Joensuu, H. (2012) Boron neutron capture therapy in the treatment of locally recurred head-and-neck cancer: final analysis of a phase I/II trial. *Int. J. Radiat. Oncol., Biol., Phys. 82*, e67−e75.

(37) McDevitt, M. R., Ma, D. S., Lai, L. T., Simon, J., Borchardt, P., Frank, R. K., Wu, K., Pellegrini, V., Curcio, M. J., Miederer, M., Bander, N. H., and Scheinberg, D. A. (2001) Tumor therapy with targeted atomic nanogenerators. *Science 294*, 1537−1540.

(38) Hawthorne, M. F. (1993) The role of chemistry in the development of boron neutron-capture therapy of cancer. *Angew. Chem., Int. Ed. Engl. 32*, 950−984.

(39) Tomalia, D. A., and Frechet, J. M. J. (2002) Discovery of dendrimers and dendritic polymers: A brief historical perspective. *J. Polym. Sci., Polym. Chem. 40*, 2719−2728.

(40) Gillies, E. R., and Frechet, J. M. J. (2005) Dendrimers and dendritic polymers in drug delivery. *Drug Discovery Today 10*, 35−43.

(41) Frechet, J. M. J. (1994) Functional polymers and dendrimers - reactivity, molecular architecture, and interfacial energy. *Science 263*, 1710−1715.

(42) Grayson, S. M., and Frechet, J. M. J. (2001) Convergent dendrons and dendrimers: from synthesis to applications. *Chem. Rev. 101*, 3819−3867.

(43) Ihre, H. R., De Jesus, O. L. P., Szoka, F. C., and Frechet, J. M. J. (2002) Polyester dendritic systems for drug delivery applications: Design, synthesis, and characterization. *Bioconjugate Chem. 13*, 443−452.

(44) Padilla De Jesús, O. L., Ihre, H. R., Gagne, L., Fréchet, J. M. J., and Szoka, F. C. (2002) Polyester dendritic systems for drug delivery applications: in vitro and in vivo evaluation. *Bioconjugate Chem. 13*, 453−461.

(45) van der Poll, D. G., Kieler-Ferguson, H. M., Floyd, W. C., Guillaudeu, S. J., Jerger, K., Szoka, F. C., and Frechet, J. M. (2010) Design, synthesis, and biological evaluation of a robust, biodegradable dendrimer. *Bioconjugate Chem. 21*, 764−773.

(46) Almutairi, A., Rossin, R., Shokeen, M., Hagooly, A., Ananth, A., Capoccia, B., Guillaudeu, S., Abendschein, D., Anderson, C. J., Welch, M. J., and Frechet, J. M. J. (2009) Biodegradable dendritic positron-emitting nanoprobes for the noninvasive imaging of angiogenesis. *Proc. Natl. Acad. Sci. U. S. A. 106*, 685−690.

(47) Newkome, G. R., Moorefield, C. N., and Vögtle, F. (2008) *Dendritic Molecules: Concepts, Syntheses, Perspectives*, p 272, Wiley.

(48) Tomalia, D. A., and Durst, H. D. (1993) Genealogically directed synthesis - starburst cascade dendrimers and hyperbranched structures. *Top. Curr. Chem. 165*, 193−313.

(49) Wooley, K. L., Hawker, C. J., and Frechet, J. M. J. (1991) Polymers with controlled molecular architecture: control of surface functionality in the synthesis of dendritic hyperbranched macromolecules using the convergent approach. *J. Chem. Soc., Perkin Trans. 1*, 1059−1076.

(50) Gillies, E. R., and Frechet, J. M. J. (2002) Designing macromolecules for therapeutic applications: Polyester dendrimer-poly(ethylene oxide) "bow-tie" hybrids with tunable molecular weight and architecture. *J. Am. Chem. Soc. 124*, 14137−14146.

(51) Heying, T. L., Clark, S. L., Hillman, M., Goldstein, H. L., Polak, R. J., Mangold, D. J., Szymansk, J. W., and Ager, J. W. (1963) A new series of organoboranes 0.1. carboranes from reaction of decaborane with acetylenic compounds. *Inorg. Chem. 2*, 1089−&.

(52) Kusari, U., Li, Y. Q., Bradley, M. G., and Sneddon, L. (2004) Polyborane reactions in ionic liquids: New efficient routes to functionalized decaborane and o-carborane clusters. *J. Am. Chem. Soc. 126*, 8662−8663.

(53) Bregadze, V. I. (1992) Dicarba-closo-dodecaboranes C2b10h12 and their derivatives. *Chem. Rev. 92*, 209−223.

(54) Valliant, J. F., Guenther, K. J., King, A. S., Morel, P., Schaffer, P., Sogbein, O. O., and Stephenson, K. A. (2002) The medicinal chemistry of carboranes. *Coord. Chem. Rev. 232*, 173−230.

(55) Yamamoto, Y. (1997) In *Advances in Chemistry* (Siebert, W., Ed.) p 281, The Royal Society of Chemistry, Cambridge, UK.

(56) Armspach, D., Cattalini, M., Constable, E. C., Housecroft, C. E., and Phillips, D. (1996) Boron-rich metallodendrimers - Mix-and-match assembly of multifunctional metallosupramolecules. *Chem. Commun.*, 1823−1824.

(57) Barth, R. F., Adams, D. M., Soloway, A. H., Alam, F., and Darby, M. V. (1994) Boronated starburst dendrimer monoclonal-antibody immunoconjugates - evaluation as a potential delivery system for neutron-capture therapy. *Bioconjugate Chem. 5*, 58−66.

(58) Dash, B. P., Satapathy, R., Bode, B. P., Reidl, C. T., Sawicki, J. W., Mason, A. J., Maguire, J. A., and Hosmane, N. S. (2012) "Click" chemistry-mediated phenylene-cored carborane dendrimers. *Organometallics 31*, 2931−2935.

(59) Nemoto, H., Cai, J. P., and Yamamoto, Y. (1994) Synthesis of a water-soluble o-carbaborane bearing a uracil moiety via a palladium-catalyzed reaction under essentially neutral conditions. *J. Chem. Soc., Chem. Commun.*, 577−578.

(60) Nemoto, H., Wilson, J. G., Nakamura, H., and Yamamoto, Y. (1992) Polyols of a cascade type as a water-solubilizing element of carborane derivatives for boron neutron-capture therapy. *J. Org. Chem. 57*, 435−435.

(61) Nunez, R., Gonzalez, A., Vinas, C., Teixidor, F., Sillanpaa, R., and Kivekas, R. (2005) Approaches to the preparation of carborane-containing carbosilane compounds. *Org. Lett. 7*, 231−233.

(62) Parrott, M. C., Marchington, E. B., Valliant, J. F., and Adronov, A. (2005) Synthesis and properties of carborane-functionalized aliphatic polyester dendrimers. *J. Am. Chem. Soc. 127*, 12081−12089.

(63) Qualmann, B., Kessels, M. M., Musiol, H. J., Sierralta, W. D., Jungblut, P. W., and Moroder, L. (1996) Synthesis of boron-rich lysine dendrimers as protein labels in electron microscopy. *Angew. Chem., Int. Ed. 35*, 909−911.

(64) Thomas, J., and Hawthorne, M. F. (2001) Dodeca(carboranyl)-substituted closomers: toward unimolecular nanoparticles as delivery vehicles for BNCT. *Chem. Commun.*, 1884−1885.

(65) Yao, H. J., Grimes, R. N., Corsini, M., and Zanello, P. (2003) Polynuclear metallacarborane-hydrocarbon assemblies: Metallacarborane dendrimers. *Organometallics 22*, 4381−4383.

(66) Mollard, A., and Zharov, I. (2006) Tricarboranyl pentaerythritol-based building block. *Inorg. Chem. 45*, 10172−10179.

(67) Yarmoluk, S. M., Kryvorotenko, D. B., and Kovalska, V. B. (2001) Interaction of cyanine dyes with nucleic acids. XX. New methods for the preparation of fluorescent probes based on

benzothiazol-4-[2,6-dimethylpyridinium] cyanine dyes. *Dyes Pigm. 48,* 165−172.

(68) Yarmoluk, S. M., Kostenko, A. M., and Dubey, I. Y. (2000) Interaction of cyanine dyes with nucleic acids. Part 19: new method for the covalent labeling of oligonucleotides with pyrylium cyanine dyes. *Bioorg. Med. Chem. Lett. 10,* 2201−4.

(69) Shindy, H. A. (2012) Basics, mechanisms and properties in the chemistry of cyanine dyes: a review paper. *Mini-Rev. Org. Chem. 9,* 352−360.

(70) Tatikolov, A. S. (2012) Polymethine dyes as spectral-fluorescent probes for biomacromolecules. *J. Photochem. Photobiol., C 13,* 55−90.

(71) Vanderplas, H. C. (1978) S(N)(Anrorc) mechanism - new mechanism for nucleophilic-substitution. *Acc. Chem. Res. 11,* 462−468.

(72) Reynhardt, E. C. (1986) C-13, B-10, and B-11 NMR IN O-Carborane. *J. Magn. Reson. 69,* 337−343.

(73) Ediz, V., Lee, J. L., Armitage, B. A., and Yaron, D. (2008) Molecular engineering of torsional potentials in fluorogenic dyes via electronic substituent effects. *J. Phys. Chem. A 112,* 9692−9701.

(74) Olsen, S., and McKenzie, R. H. (2012) A two-state model of twisted intramolecular charge-transfer in monomethine dyes. *J. Chem. Phys. 137.*

(75) Graber, M. L., Dilillo, D. C., Friedman, B. L., and Pastorizamunoz, E. (1986) Characteristics of fluoroprobes for measuring intracellular pH. *Anal. Biochem. 156,* 202−212.

(76) Han, J. Y., and Burgess, K. (2010) Fluorescent indicators for intracellular pH. *Chem. Rev. 110,* 2709−2728.

(77) Klonis, N., and Sawyer, W. (1996) Spectral properties of the prototropic forms of fluorescein in aqueous solution. *J. Fluoresc. 6,* 147−157.